

Design and development of a compact thermal air sterilizer with recycling: Experiment, Modelling & Simulation

Amarendra Kumar Gupta*, Sunil Kumar Thamida**

*(*Department of Chemical Engineering, Indian Institute of Technology Tirupati, Andhra Pradesh, India*
Email: ch20d501@iittp.ac.in)

** (*Department of Chemical Engineering, Indian Institute of Technology Tirupati, Andhra Pradesh, India*
Email: sunil76@iittp.ac.in)

ABSTRACT

The escalating threat of airborne viral pathogens, including SARS-CoV-2 and Nipah, underscores the critical need for robust air sterilization technologies, with thermal deactivation via dry heating emerging as a promising approach due to its capacity to inactivate viruses at 60°C within seconds. This study presents the design and evaluation of a thermal air sterilizer incorporating wall heating and air recycling, optimized through computational fluid dynamics simulations (COMSOL Multiphysics) to minimize temperature variations and identify regions of suboptimal heating within recycling chambers. Experimental validation of the prototype demonstrated rapid start-up times, sustained operational stability, and a significant reduction in microbial load, as evidenced by optical density measurements of 0.001 units for sterilized air compared to 2 units for untreated ambient air. These results, consistent with simulation-derived thermal profiles, confirm the system's efficacy in achieving near-complete microbial deactivation while maintaining structural and functional reliability. The findings highlight the potential of this thermally driven sterilization technology to enhance air quality in high-risk environments, offering a scalable solution for mitigating airborne infection transmission, with future research directed toward operational optimization and diverse application scenarios.

Keywords - Airborne virus; Dry Heat Sterilization; Hospital disinfection; Recycle; Numerical CFD Simulation.

Date of Submission: 02-03-2025

Date of acceptance: 12-03-2025

I. INTRODUCTION

Heating of air has many applications like room heating in winter and cold places, calcining, drying, melting, preheating, sterilizing etc. Out of these sterilizing the air is the most relevant application. Sterilization is the process of removing, killing, or deactivating all forms of microorganisms like bacteria, prions, fungi, and unicellular eukaryotic organisms in or on a surface or fluid [1]. Sneezing, Respiration, fuel-based vehicles, industries are mainly the source of pollutants responsible for transmission of airborne viruses [2]. Flowing air is used in the food industry for pneumatic conveying, manufacturing of foodstuff, packing and filling etc. where it comes in direct contact with foodstuffs, which, when it is not sterilized, may contaminate it and cause health problems [3–5]. In medical sectors, where patients are in immunocompromised conditions the slightly contaminated air can cause severe danger [6]. These bacteria and viruses spread through cough sneezes from one receptor to another in the form of aerosols. One way to protect the receptor from this is to either make their immune strong by vaccination or isolate

them. Many papers were published from China and India which recommended to use traditional plants to boost the immune system [7]. Apart from this, other applications are in biosafety laboratories where there is a danger of bacterial growth, in industries, schools and colleges, commercial and public places, residential homes sterilization is required [8]. The lifetime of such airborne microbes continued to be around several hours thus imposing severe threat even in the post-lockdown period [2].

Sterilization can be done through sterile filtration, radiation sterilization like photothermal sterilization [9], chemical sterilization like photo electrocatalytic sterilization [10] or by using heat [11]. All these processes of sterilization have some disadvantages like in the case of Sterile filtration: Only microbes having certain dimensions can be sterilized, and sterilization of filter by steam is required at regular intervals [12]. Radiation sterilization: It may affect the material properties, may affect the worker's health from radiation exposure as well as requires much more electrical energy [13]. Chemical sterilization: It is toxic, flammable, and carcinogenic to humans as well as only solids can be sterilized with this method

[14,15]. Heat sterilization: ‘steam sterilization’ causes rusting of steel objects, ‘flaming sterilization’ can’t be used for large objects, ‘incineration’ can cause emission of polluting gases etc. Various techniques of thermal air sterilization were reviewed by [16].

Therefore, various new techniques of sanitization need to be modified with respect place, time and prevailing climatic conditions. Various preventive measures such as indoor air purifier, ventilation system, aerosol separator etc. can be used to control the airborne transmission of these viruses [2]. Out of various means of sterilization by heat, dry heat sterilization is one of them [17]. It is the first method of sterilization which can be efficiently used for air sterilization. There are few literature articles indicating the temperature of medium vs time of deactivation of SARS COVID-19 [18,19]. The curve is plotted in **Fig. 1**, which shows that for a temperature 55°C-60°C, it requires very less time for the de-activation of the virus [19].

With this very basic knowledge of dry heat sterilization technique, one air sterilizer was designed. The same prototype was simulated in COMSOL Multiphysics software. The internal flow and heat transfer was studied with this CFD-based software tool for nonisothermal turbulent flow based on Reynolds Average Navier-Stokes (RANS) equation [20].

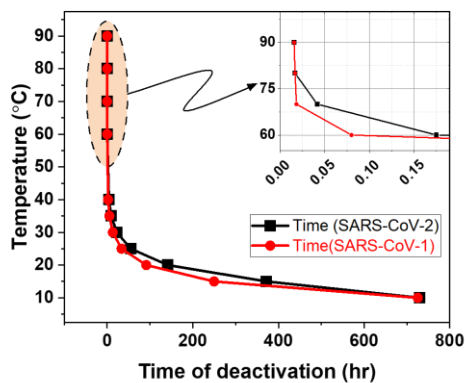


Fig. 1. Thermal deactivation of SARS-CoV-19 virus w.r.t. time.

II. DESIGN AND EXPERIMENT ON THE DEVELOPED PROTOTYPE OF THE AIR STERILIZER

The proposed process flowsheet of sterilization is represented in **Fig. 2**. The suction requires an air blower. Heating requires a surface heating mantle. The retention and recycling require sufficient volume in the chamber. In addition to these processes, there will be instruments like valves and sensors which will help us in monitoring and

optimizing the operating conditions such that an exit air temperature of 60°C can be maintained.

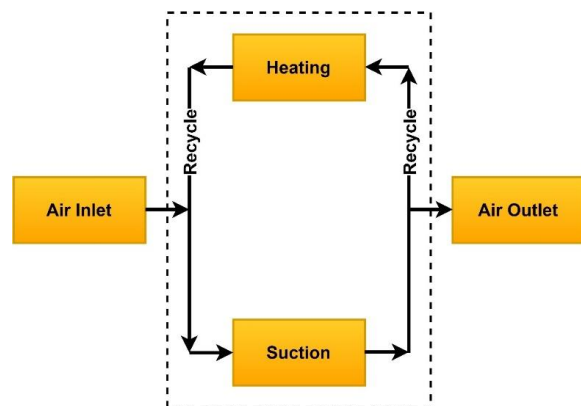


Fig. 2. Schematic of process flow sheet for dry heat sterilization.

Based on the proposed process flow sheet, an actual prototype is developed as shown in **Fig. 3**. This prototype contains an inlet, outlet, blower, and wall heater with a recycling chamber. The capacity of the heater and blower are 150 watts each. Lateral surface area of wall heater is 0.033 m² (diameter = 5 cm, length of cylinder = 21 cm). So, the Heater capacity per unit surface area is 4545.45 W/m². The entire prototype along with the temperature sensor and control panel is covered with a stainless-steel sheet of a thickness of 2.5 mm, which provides a good heat shield and elegant look from the outside. The prototype is mounted on a trolley with wheels for easy portability. The internal schematic is shown in **Fig. 4**.

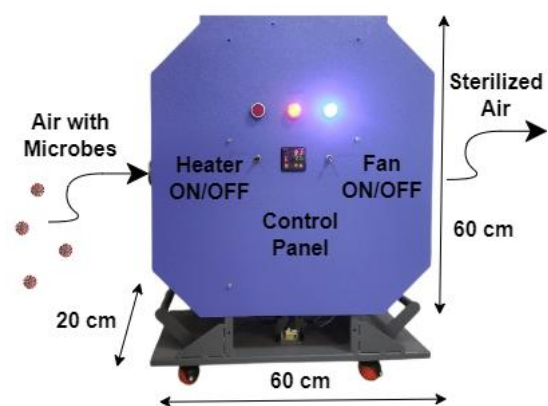


Fig. 3. Image of the developed actual prototype of thermal air sterilizer (front view).

Initially, all the switches (mains, blower, heater) are in the OFF position. The main plug must be connected to a power supply and the blower and heater are switched ON simultaneously. The time to

reach the set point varies with varying inlet air flow rates by partially opening or closing the inlet pipe.

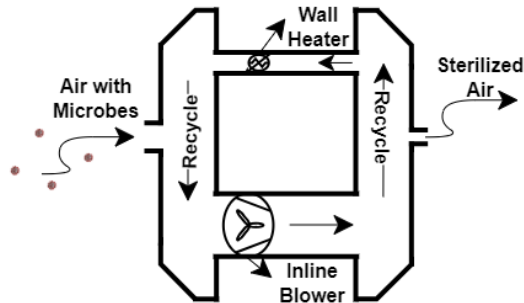
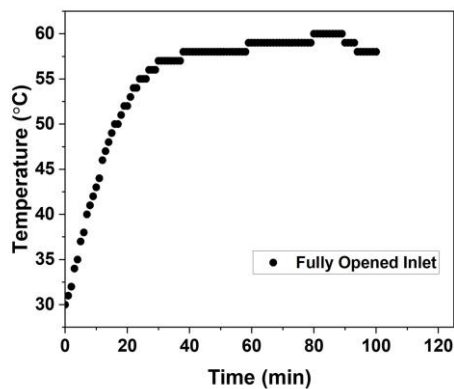


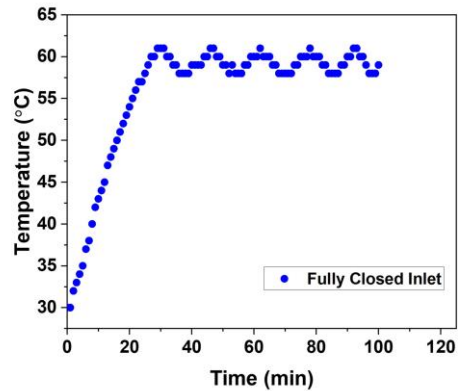
Fig. 4. Schematic of proposed thermal air sterilizer design.

Two experiments were performed by varying inlet flowrate to see how the machine is responding. For this, in the first run, the inlet is fully open. In the second run, the inlet is fully closed. Since, in the fully closed inlet, complete recycling is taking place, it is expected that it would take a minimum time to reach the set point temperature. The result of this experiment is shown in **Fig. 5**. **Fig. 5(a)** shows the result for a fully open inlet which is taking more than 60 minutes to reach the set point. But a fully closed inlet is taking 25 minutes as shown in **Fig. 5(b)**.

The temperature of the heater surface is measured by using HTC MT- 4 Digital Infrared Thermometer, as shown in **Fig. 6(a)**. The resolution of this IR thermometer is 0.1°C and it can measure temperature in the range of -50°C to 550°C . Outlet velocity is also measured by using Professional Instruments Anemometer, as shown in **Fig. 6(b)**. This also has an LCD and resolution of 0.1 m/s . It measures the velocity in the range of 0 to 30 m/s . The outflow velocity is around 5 m/s at open inlet.



(a)



(b)

Fig. 5. Time required to reach the set point (60°C) for (a) fully opened inlet and (b) fully closed inlet.

Velocity is measured at the outlet in both fully opened and fully closed inlet conditions as shown in **Table 1**. The flowrate based on this velocity and the outlet cross-section comes out to be around $8\text{ m}^3/\text{hr}$. So, if there is a room of $3 \times 3 \times 3\text{ m}^3$, the time that this machine will take to sterilize it will be around 3 hours. When the inlet is fully closed the velocity at the outlet is very minimal, depicting there are no leaks in the machine because law of conservation of mass is satisfied. The negligible velocity at the outlet when the inlet is fully closed also increases the number of recycling and thus achieves a steady state earlier. Some velocity detectable is due to recirculation and backflow.



Fig. 6. Image of the used (a) IR digital thermometer (b) anemometer.

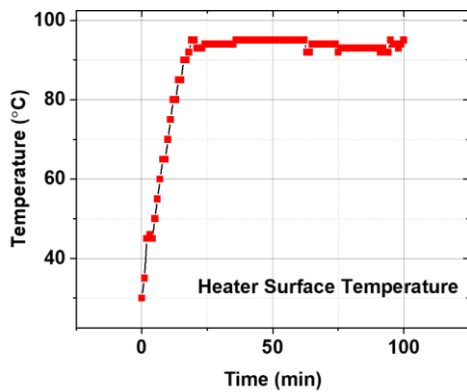


Fig. 7. Surface temperature of heater w.r.t. time.

Table 1. Air velocity measured through anemometer.

Case	Velocity magnitude (m/s)
Fully opened inlet	5
Fully closed inlet	0.2

III. MODELLING AND SIMULATION

The governing equations are formulated for air heating and flow based on the weakly compressible, Newtonian fluid and unsteady-state conditions. Based on the inflow velocity, which is 4.5 m/s, and let the length scale L equal to the diameter of the inlet, the Reynolds number can be calculated using Eq. (1) [21].

$$Re = \frac{U \cdot L}{\nu} = \frac{4.5 \cdot 0.05}{1.6 \cdot 10^{-5}} = 14000 \quad (1)$$

The high Reynolds number indicates that the flow is turbulent [21,22], and a turbulence model must be applied. The application of constant wall heat flux is responsible for non-isothermal flow [23]. The fundamental basis for many flows of engineering interest requires the solution of continuity and the Navier-Stokes equations [24,25], which can be expressed as in Eq. (2) and Eq. (3) respectively.

Continuity equation:

$$\frac{\partial \rho}{\partial t} + \frac{\partial}{\partial x_i} (\rho u_i) = 0 \quad (2)$$

Navier-Stokes equation:

$$\frac{\partial}{\partial t} (\rho u_i) + \frac{\partial}{\partial x_j} (\rho u_i u_j) = -\frac{\partial p}{\partial x_i} + \frac{\partial}{\partial x_j} \left(\mu \frac{\partial u_i}{\partial x_j} \right) \quad (3)$$

Eq. (2) and Eq. (3) are applicable for laminar as well turbulent flow [26]. However, for the turbulent flow, every velocity and pressure term in Eq. (2) and Eq. (3) are varying in time due to the turbulent fluctuations [27].

For analysis of turbulent flow, many numerical methodologies have been used such as Reynolds-Averaged Navier-Stokes (RANS) model [28–30], Direct-Numerical Simulation (DNS) [31] and Large Eddy Simulation (LES) [32,33] etc. DNS is the most accurate approach for turbulent flow simulations and pursues a thorough three-dimensional resolution of all the turbulent scales in time and space by solving the Navier-Stokes equations. However, currently, it is only applicable for simple geometry with low Reynolds numbers and is very expensive. LES is useful where large eddies are forming in the turbulent flow. LES is less expensive than DNS, however, the number of computational resources and efforts are still too large for most practical applications [26]. RANS model is an alternative approach to simulate turbulent flow. It has been working as a backbone in the modern CFD method for the last few decades for simulating turbulent flow due to its less computing cost and affordable use. Apart from this, NS equations are very sensitive to initial conditions and cannot address a wide range of length scales and time scales [32]. These complexities can be reduced by considering the statistical average form of NS equations or RANS equations.

The turbulent flow causes significant fluctuation of flow properties like velocity, pressure, temperature and even density (for compressible flow). To obtain governing equation which includes these fluctuations, the flow properties are decomposed into average and fluctuation components like in Eq. (4). The time average of the fluctuating component is zero ($\overline{u'} = 0$) and the average value is expressed as in Eq. (5).

$$u = \bar{u} + u' \quad (4)$$

$$\overline{u(x)} = \lim_{\Delta t \rightarrow \infty} \int_{t_1}^{t_1 + \Delta t} u(x, t) dt \quad (5)$$

By substituting Eq. (4) into Eq. (2) and Eq. (3), the Eq. (6) and Eq. (7) are obtained.

$$\frac{\partial \rho u_j}{\partial x_i} = 0 \quad (6)$$

$$\frac{\partial \rho u_i}{\partial t} + \frac{\partial}{\partial x_j} (\rho u_i \bar{u}_j) = -\frac{\partial p}{\partial x_i} + \frac{\partial}{\partial x_j} \left(\mu \frac{\partial \bar{u}_i}{\partial x_j} \right) - \frac{\partial}{\partial x_j} (\rho \overline{u'_i u'_j}) \quad (7)$$

The left-hand side of this Eq. (7) represents a time-dependent change in the mean momentum of the working fluid. This change in mean momentum is equal to the right-hand side mean pressure field, the viscous stresses and one more term. Eq. (7) is a RANS equation which is very identical to Eq. (3) apart from one additional term $\overline{u'_i u'_j}$. This term is known as the Reynolds stress, and it is expressed in Eq. (8).

$$\overline{u'_i u'_j} = \begin{bmatrix} \overline{u'^2} & \overline{u'v'} & \overline{u'w'} \\ \overline{v'u'} & \overline{v'^2} & \overline{v'w'} \\ \overline{w'u'} & \overline{w'v'} & \overline{w'^2} \end{bmatrix} \quad (8)$$

The diagonal terms are denoted as normal stress, whereas symmetric upper and lower diagonals are denoted as shear stress. Because of this, Reynold's averaging has created six independent elements. The six independent elements are the Reynold normal stresses ($\overline{u'^2}, \overline{v'^2}, \overline{w'^2}$) and Reynold shear stresses ($\overline{u'v'}, \overline{v'w'}, \overline{u'w'}$), and it is called a closure problem. Thus, to close this problem, modelling Reynold-stresses in terms of mean flow quantities is needed.

A linear relationship between turbulent or Reynolds stresses and mean strain was proposed by Boussinesq [34]. This was the first turbulent-viscosity approximation based on the analogy with the kinematic viscosity in Newton's law for laminar flow. It is expressed as in Eq. (9).

$$\tau_{ij} = \rho \overline{u'_i u'_j} = \frac{2}{3} \rho k \delta_{ij} - \mu_t \left(\frac{\partial \overline{u}_i}{\partial x_j} + \frac{\partial \overline{u}_j}{\partial x_i} \right) \quad (9)$$

The turbulence kinetic energy is expressed as in Eq. (10). By substituting Eq. (8) into Eq. (7), the equation becomes Eq. (11). The isentropic part of the Reynolds-stress tensor is blended into the pressure term as in Eq. (12). The common turbulence models are classified based on the number of additional transport equations that need to be solved along with the RANS equations. One equation RANS models were specifically developed to solve one turbulent transport equation, like turbulent kinetic energy. Two equation models introduce two additional transport equations and two dependent variables: the turbulent kinetic energy, k , and the turbulent dissipation rate, ϵ . The k - ϵ model, proposed by Launder and Spalding [35], is one of the most used turbulence models for industrial applications. It is relatively robust and computationally inexpensive compared to more advanced turbulence models.

$$k = \frac{1}{2} \overline{u'_i u'_j} = \overline{u_1'^2} + \overline{u_2'^2} + \overline{u_3'^2} \quad (10)$$

$$\frac{\partial \overline{u}_i}{\partial t} + \frac{\partial}{\partial x_j} (\overline{u}_i \overline{u}_j) = -\frac{1}{\rho} \frac{\partial \overline{p}^*}{\partial x_i} + \frac{\partial}{\partial x_j} \left[(\mu + \mu_t) \frac{\partial \overline{u}_i}{\partial x_j} \right] \quad (11)$$

$$\overline{p}^* = \overline{p} + \frac{2k}{3} \quad (12)$$

One major reason the k - ϵ model is inexpensive is that it employs wall functions to describe the flow close to walls instead of resolving the very steep gradients there. It leads to stable calculations and is relatively simple to implement. The turbulent viscosity is modelled as in Eq. (13). The transport equations for the standard k - ϵ is expressed as in Eq. (14) and Eq. (15). In Eq. (13), left-hand side terms indicate a change of turbulent kinetic energy w.r.t. time as well as space i.e., a combination of unsteady state change of 'k' along with convective transport. On the right-hand side, the terms represent diffusive transport, rate of production and rate of destruction of turbulent kinetic energy respectively. Similarly, Eq. (14) represents a change in turbulent dissipation rate. The standard values of model coefficients [36] are given in Eq. (16).

$$\mu_t = \rho C_\mu \frac{k^2}{\epsilon} \quad (13)$$

$$\frac{\partial}{\partial t} (\rho k) + \frac{\partial}{\partial x_j} (\rho u_j k) = \frac{\partial}{\partial x_j} \left[\left(\mu + \frac{\mu_t}{\sigma_k} \right) \frac{\partial k}{\partial x_j} \right] - \rho \overline{u'_i u'_j} \frac{\partial u_j}{\partial x_i} - \rho \epsilon \quad (14)$$

$$\frac{\partial}{\partial t} (\rho \epsilon) + \frac{\partial}{\partial x_j} (\rho u_j \epsilon) = \frac{\partial}{\partial x_j} \left[\left(\mu + \frac{\mu_t}{\sigma_\epsilon} \right) \frac{\partial \epsilon}{\partial x_j} \right] + C_{1\epsilon} \frac{\epsilon}{k} \rho \overline{u'_i u'_j} \frac{\partial u_j}{\partial x_i} - C_{2\epsilon} \frac{\epsilon^2}{k} \quad (15)$$

$$C_\mu = 0.09, C_{1\epsilon} = 1.44, C_{2\epsilon} = 1.92, \sigma_k = 1.0, \sigma_\epsilon = 1.3 \quad (16)$$

Based on the beforementioned formulations and conditions mentioned in **Table 2** and **Table 3**, the simulation is performed by using COMSOL Multiphysics software. This is CFD-based software and uses the finite element method (FEM) for simulation. FEM is a numerical technique used to solve complex engineering and physical problems governed by partial differential equations. It discretizes a continuous domain into smaller, simpler elements (e.g., triangles, tetrahedra) and approximates solutions using shape functions to interpolate variables within each element. FEM enables accurate modelling of structures, heat transfer, fluid flow, and electromagnetic phenomena, particularly for irregular geometries and nonlinear

material behaviours. The geometry is designed in '2D Model Wizard', as shown in Fig. 8, by using 'Rectangle', 'Bezier Polygon', 'difference' and 'form union' options available in the 'Geometry' menu. 'Internal fan' is used to provide suction from the inlet and a constant 'Inward Heat Flux' is given to mimic the wall heater. All boundaries are 'walls' in Fig. 8 except the inlet, the outlet, and the internal fan. 'Component Coupling' is being used for the temperature ON/OFF control, to bound the inward heat flux according to the outlet temperature of the prototype. Component Coupling in COMSOL Multiphysics enables interaction between variables or fields across separate components or physics interfaces in a model.

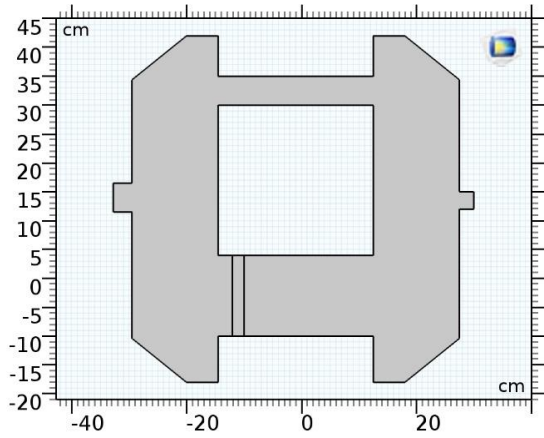


Fig. 8. 2D geometry of prototype designed in '2D Model Wizard' in COMSOL Multiphysics software.

Reference and ambient temperature and pressure are taken as 293.15 K and 1 atm respectively. Since 2D geometry is being used, out-of-plane thickness is taken as 1 m. The ambient wind is considered to have zero relative humidity and is stagnant. Fluid is taken to be air, and all its properties are given in Table 2. A thin layer of stainless is also considered which is present in our prototype and it's all properties are mentioned in Table 2.

Table 2. Properties of fluid and thin external layer of the prototype.

Fluid Properties (Air)	Value	Unit
Dynamic viscosity	10^{-5}	Pa.s
Thermal conductivity	0.025	W/(m.K)

Density	1	Kg/m ³
Heat capacity at constant pressure	1000	J/(Kg.K)
Ratio of specific heat	1	-
Thin Layer Properties (Stainless-Steel)		
Thickness	0.025	m
Layer thermal conductivity	15	W/(m.K)
Layer density	8000	Kg/m ³
Layer heat capacity	450	J/(Kg.K)

Inlet, Outlet and Wall boundary conditions are given in Table 3. At the outlet, thermal insulation is considered. The most suitable values of two parameters, i.e., pressure drop through the interior fan and general inward heat flux were taken as shown in Table 3.

Table 3. Boundary conditions and two adjustable parameters.

Inlet Boundary Condition	Value	Unit
Temperature	303.15	K
Pressure	101325	Pa
Outlet Boundary Condition		
Pressure	101325	Pa
$-n \cdot q = 0$ (Thermal insulation)	-	-

Wall Boundary Condition		
No slip	-	-
$-n \cdot q = 0$ (Thermal insulation)	-	-
Adjustable Parameters		
Pressure-drop through Interior fan	25	Pa
General inward heat flux	4450	W/m ²

IV. RESULTS AND DISCUSSIONS

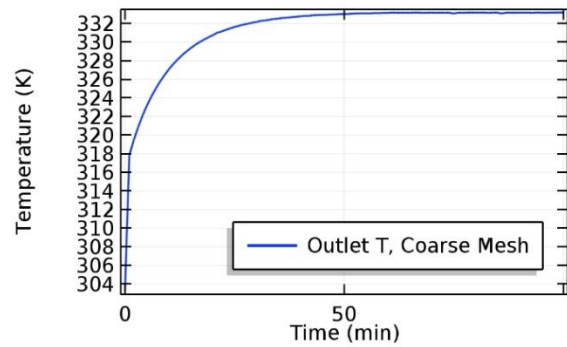
Mesh sensitivity analysis

Mesh sensitivity analysis is a critical step in finite element analysis (FEA) to ensure simulation results are independent of the discretization of the computational mesh. It involves refining the mesh iteratively. By systematically refining meshes and monitoring convergence, users gain confidence in their simulations. Leveraging COMSOL's adaptive tools and best practices streamlines this process, making it integral to robust numerical modeling. For meshing in this case, physics-controlled meshing was adopted. And the results were analyzed and compared for two cases i.e. for coarse and coarser meshes. The mesh discretizes a geometry into elements, and its quality directly impacts solution accuracy. A coarse mesh may under resolve gradients, while an overly refined mesh increases computational cost. Mesh sensitivity analysis validates that results are reliable and not artifacts of mesh choice. As shown in Fig. 9, the exit temperature for different mesh types i.e., coarse, and coarser mesh is not varying so much. So, to avoid more computational time and energy loss 'Coarser Mesh' is adopted as optimum mesh in this case.

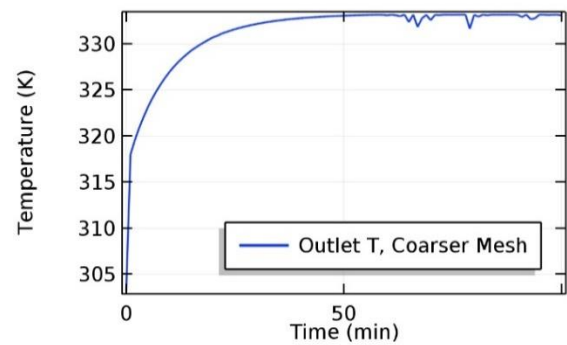
Temperature Field

To observe how temperature is varying in the outlet chamber and on the surface of the heater, the 'More Derived Variables' drop-down menu was used from the 'Results' menu of the COMSOL graphical user interface. Line average variation of temperature w.r.t. time first at the outlet and then on

the heater surface was chosen. Fig. 10(a) and Fig. 10(c) are for fully open inlets, and Fig. 10(b) and Fig. 10(d) are for fully closed inlets. Fig. 10(a) and Fig. 10(b) depict that in a fully opened inlet condition, the time required for outlet temperature to reach the set point is 60 minutes while in the case of a fully closed condition it is around 25 minutes.



(a)

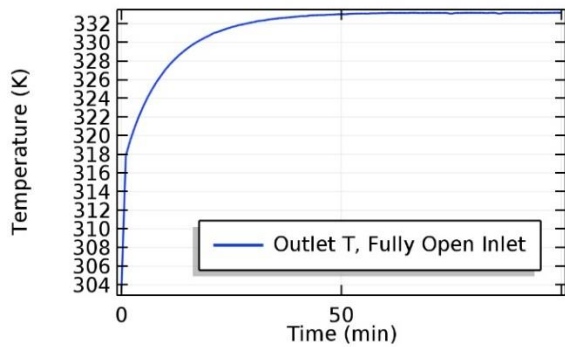


(b)

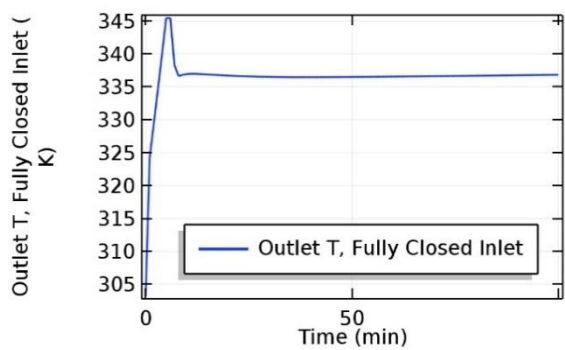
Fig. 9. Exit temperature and time required to reach a steady state for various mesh types: (a) coarse and (b) coarser mesh.

The prediction is not very accurate at initiation but at the steady state the predictions are converging towards more reliable results. The temperature at the steady state is not less than 60°C at the outlet. This means that at least 60°C environment is available throughout the machine, which can lead to better sterilization. Further the temperature field near the wall heater is more than 90°C in case of fully open inlet condition. This shows that if the microbes pass through it once, its probability of getting deactivated is very high. Since there will be cell wall rupture due to such elevated

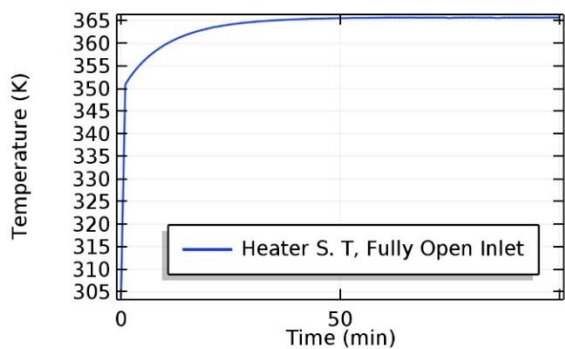
heater wall temperature. Because there is recycling of the air the probability that the microbes will pass through it is very certain. Only about 10% of the air is getting out at the outlet and all 90% of the air is recycled back towards the heater pipe and undergoes further heating.



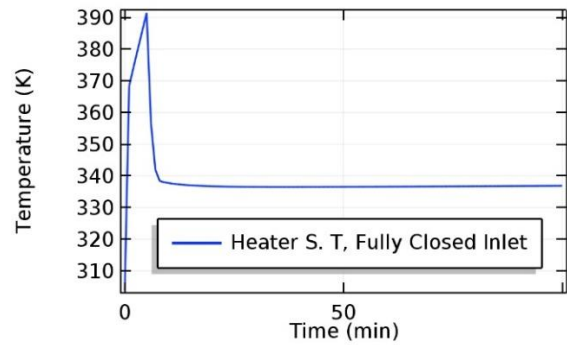
(a)



(b)



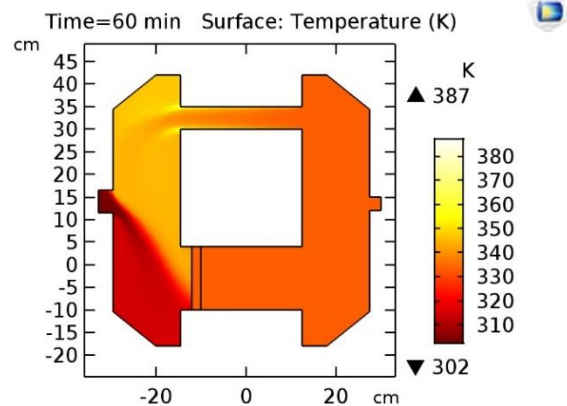
(c)



(d)

Fig. 10. Average temperature vs time: (a) At outlet for fully open condition. (b) At outlet for fully closed condition. (c) At heat surface for fully open condition. (d) At heater surface for fully closed condition.

Fig. 11 is depicting the temperature colour map and temperature contours inside the chamber at a steady state. The maximum temperature in the case of the fully open inlet is 387 K as shown in **Fig. 11(a)** and **Fig. 11(c)**. However, the maximum temperature attainable in the case of a fully closed inlet is 337 K as shown in **Fig. 11(b)** and **Fig. 11(d)**. The colour maps are taken at 60 minutes for fully open inlet conditions and at 25 minutes for fully closed inlet conditions, since the steady state is achieved at this time for the two respective cases. For the fully open condition the temperature variation is not only temporal but also spatial. But for fully closed inlet, the temperature variation is not so drastic. This is so, because there is continuous ambient air inlet in the first case. The highest temperature is not inside the inlet chamber.



(a)

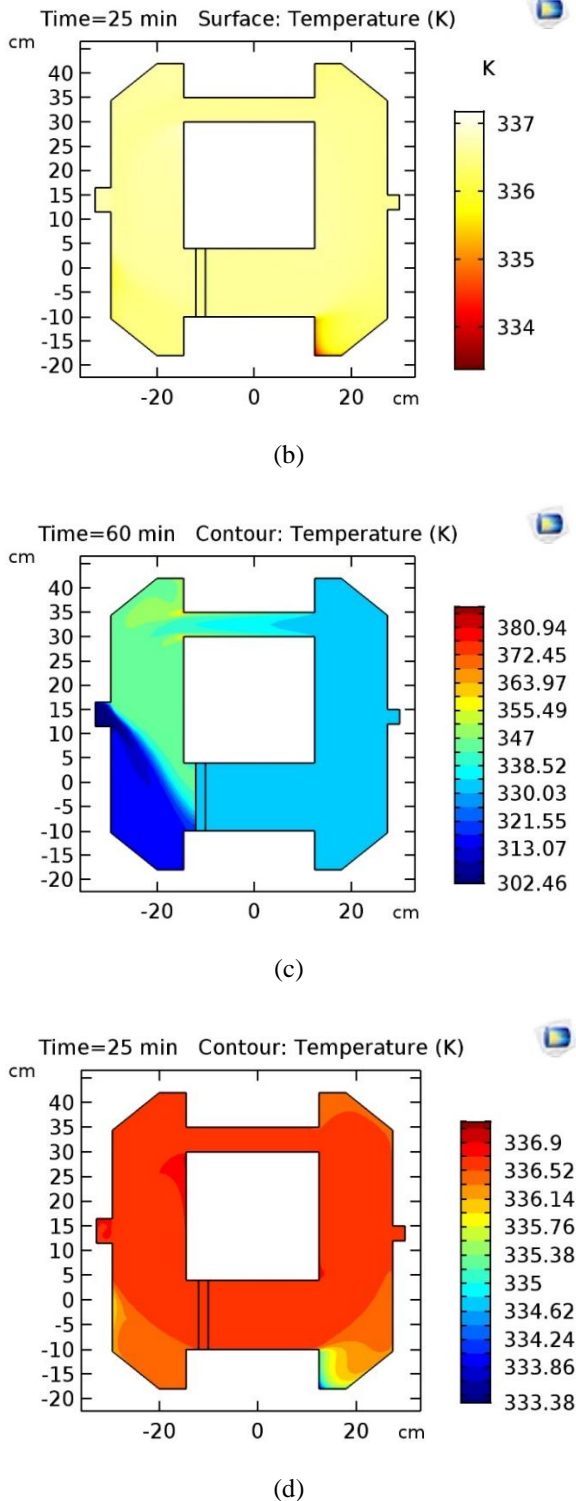


Fig. 11. Temperature colour maps and temperature contours inside the sterilizer at a steady state for: (a) & (c) fully opened and (b) & (d) fully closed inlet respectively.

Velocity Field

Fig. 12(a) and **Fig. 12(b)** depict the velocity magnitude in the whole prototype at fully opened and fully closed inlets respectively at a steady state. **Fig. 12(a)** depicts that the maximum velocity is 5 m/s, shown by the dark red colour. This red colour can also be seen at the exit of the prototype in case of a fully opened inlet. However, velocity is negligible at the exit in the case of a fully closed inlet, as per the given legend colour in **Fig. 12(b)**. This shows the complete recycling of the air.

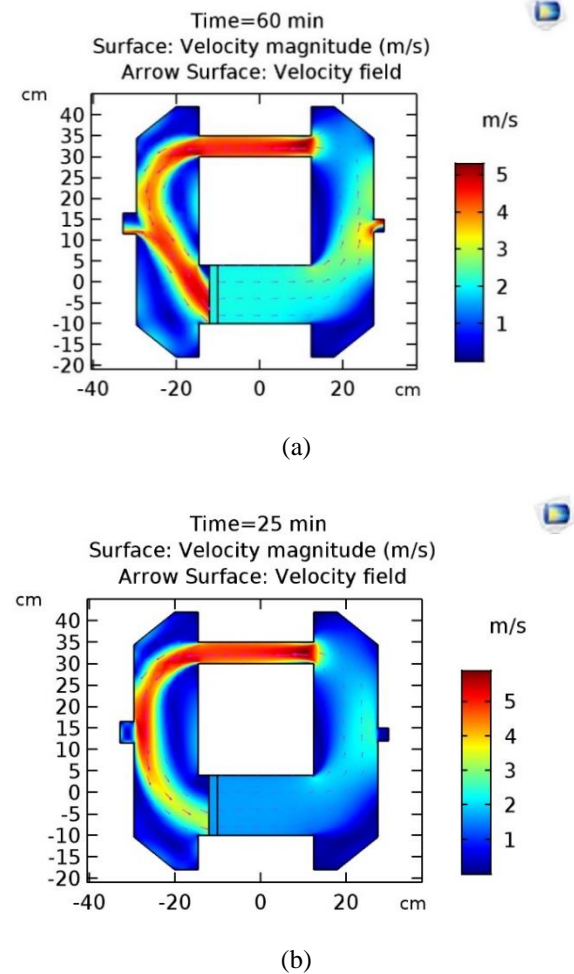


Fig. 12. Velocity colour maps inside the air sterilizer at steady state for: (a) fully opened and (b) fully closed inlet.

Simulation Validation

As described in section II, about the experiment on thermal sterilizer, where the temperature was measured in the outlet of the chamber for different inlet openings. In **Fig. 13**, temperature vs time profile was plotted for both

simulated as well as experimental studies. These plots for fully opened inlet and fully closed inlet are shown in **Fig. 13(a)** and **Fig. 13(b)** respectively. For the validation of our simulation results, Root Mean Square Error (RMSE) was calculated, and the results are given in **Table 4** by using the following formula [37].

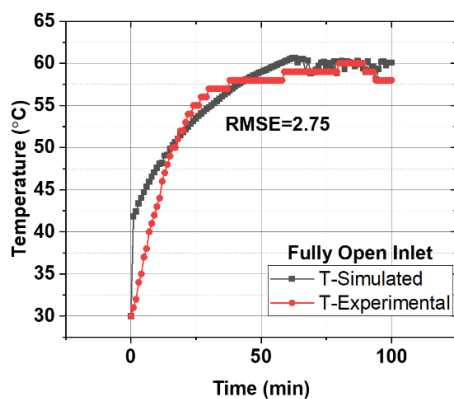
$$RMSE = \sqrt{\frac{\sum_{i=1}^N (x_i - \hat{x}_i)^2}{N}}$$

Where N is the number of all data points, x_i is the i^{th} experimental data point and \hat{x}_i is the i^{th} simulated data point.

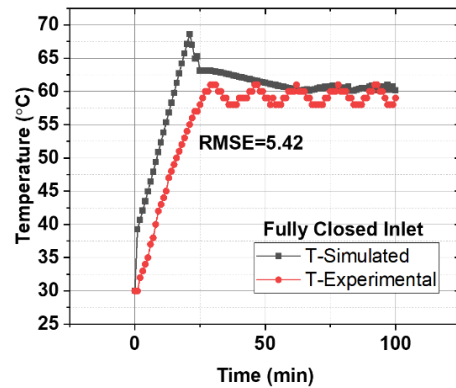
Table 4. Root-Mean-Square-Error between experimental and simulated results for outlet air temperature.

Case	RMSE
Fully opened inlet	2.75
Fully closed inlet	5.42

By observing RMSE values and **Fig. 13**, it is evident that the simulated results are matching in good agreement with the experimental results. The simulated results show the dead zones, high turbulent zones, high and low temperature zones. Hence, new drawings can be developed for the design of thermal air sterilizers using CFD software. In that new design, the two adjustable parameters can be varied to find an optimum heater and blower capacity. As well as how the shape of the machine can be varied to minimize the number of eddies.



(a)



(b)

Fig. 13. Comparison of simulation with experimental results with two adjustable parameters (heat flux and pressure drop across blower) for: (a) fully opened and (b) fully closed inlet.

The time required to reach a steady state in the case of a fully closed inlet is less as compared to a fully opened inlet condition. Because in fully closed inlet condition, complete recycling is taking place. This depicts that our prototype is working in a good manner. When a microorganism passes through this section and since its probability of collision with this highly heated surface is high, it will feel a sudden heat shock and its cell membrane may be damaged immediately within a fraction of seconds. Since we are using recycling where 90% of the air is being recycled back, there is a great probability that all the microbes present in the flow field must collide with the heater surface at least once. If they are colliding with the surface a greater number of times, they will surely be killed by heat shock provided to them suddenly in a continuous manner. The best-simulated results are obtained at a heater capacity of 4450 W/m^2 , which is very similar to the actual capacity, see **Table 5**. The unsteady-state temperature profile at heater surface, at this heater capacity is depicted in **Fig. 14**. This shows a feasible and good match with experimental data as plotted in **Fig. 7**. From **Fig. 11(a)**, it is very clear that the temperature at a steady state near the heater surface is around $365 (92 \text{ }^\circ\text{C})$ for a fully opened inlet but in the case of a fully closed **Fig. 11(b)** inlet, the temperature in an unsteady state is reaching very high but when it stabilizes it is around 60°C . By observing these results, a fully opened inlet will give better results regarding killing the microbes as compared to another case because low quality of heat shock felt by the microorganisms. And it is evident that with an increase in temperature, the time required for sterilization reduces [19].

Table 5. Actual and Simulated heater capacity.

Actual Heater Capacity	4545.45 watt/m ²
Best Simulated Results at Heater Capacity	4450 watt/m ²

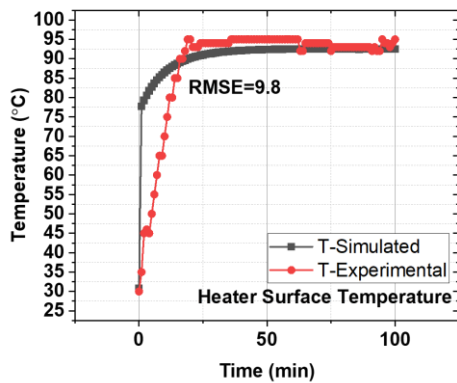


Fig. 14. Comparison of simulation with experimental results of temperature (obtained through IR thermometer) at the heater surface.

The velocity magnitude at the outlet of the prototype also matches with what was observed from the actual experiment measured with an anemometer, see **Table 6**.

Table 6. Outlet air velocity magnitude by experimental and simulated study.

Case	Experimental Velocity magnitude (m/s)	Simulated Velocity magnitude (m/s)
Fully open inlet	5	5
Fully closed inlet	0.2	0.3

By observing the flow pattern of the air inside the chamber, the shape of the prototype can be modified in future versions, so that its size will be more compact. In all these two cases the temperature

inside the chamber is higher than 60°C, which is suitable for the sterilization process of air droplets containing microbes. This temperature can be changed by changing the set-point.

Microbial Deactivation

Petri Dish method: When an agar gel plate with nutrients is exposed to contaminated air for 1min then incubated at 36°C gives rise to growth of microbial colonies. For sterile air there will not be any microbial colonies after 24hrs [21]. *Solution in a conical flask containing microbe nutrients method:* The same procedure as above is followed for growth medium in liquid. At the end of 24hrs optical density (OD600 with UV spectrophotometer) of the reagent liquid will indicate the microbial level. In almost all the tests conducted the exit air at 55°C set point has shown a turbidity or microbial level of 0.001 units against 2 units for room air as shown in **Fig. 15** and **Fig. 16**. Therefore 99.9% and above sterilization is achieved with this prototype.

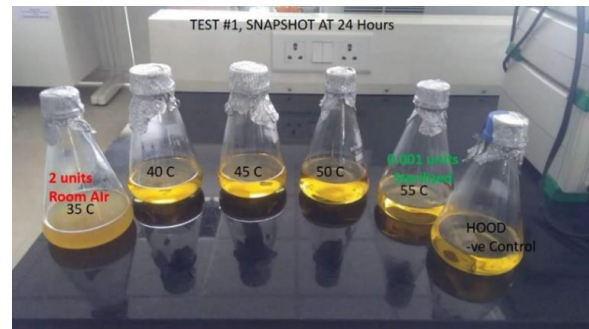


Fig. 15. Representation of turbidity due to microbial growth in nutrient growth medium.

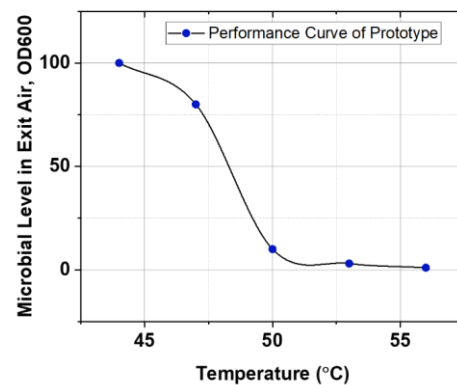


Fig. 16. Performance curve of prototype representing Optical Density w.r.t. Temperature rise measured through spectrophotometer.

V. CONCLUSION

Particularly for indoor air sterilization, a thermal air sterilizer is designed to have features of wall

heating, air blower, recycling, and control. At the end of 24 hr., the optical density (OD600 with UV spectrophotometer) of the reagent medium was checked, and it indicated a microbial level of 0.001 against 2 units for room air. And thereby microbial deactivation is happening due to the rupture of the cell membrane in only a few seconds. Its start-up time and long-term operation are studied in detail. Flow dead zones and high and low-temperature zones are identified by a simulation study performed using COMSOL CFD software. Here k- ϵ model is used based on Reynolds Average Navier-Stokes (RANS) equation for turbulent non-isothermal flow inside the chamber. This model can simulate the flow of hot air and is comparable with our results obtained from the experimental study using two adjustable parameters i.e., pressure drop through fan and heat flux. Based on the flow pattern observed from the simulation, we can adjust the shape of the prototype in future versions. It is also planned to insulate the outer surface of the heater to avoid unnecessary heat loss to the surrounding. The developed prototype demonstrates the principle of working and it can be scaled up for HVAC systems for buildings and offices for a safe environment and to protect people from the spread of the virus in the air. Because a healthy atmosphere makes the earth a better place to dwell, ensuring its future lifecycle.

ACKNOWLEDGEMENTS

We appreciate IIT Tirupati for providing all the relevant research facilities and software required for this project.

REFERENCES

- [1] J.P. Abraham, B.D. Plourde, L. Cheng, Using heat to kill SARS-CoV -2, *Rev Med Virol* 30 (2020). <https://doi.org/10.1002/rmv.2115>.
- [2] S. Mukherjee, S. Boral, H. Siddiqi, A. Mishra, B.C. Meikap, Present cum future of SARS-CoV-2 virus and its associated control of virus-laden air pollutants leading to potential environmental threat – A global review, *Journal of Environmental Chemical Engineering* 9 (2021) 104973. <https://doi.org/10.1016/j.jece.2020.104973>.
- [3] I. Dincer, Heat transfer during heat sterilization and cooling processes of canned products, *Heat and Mass Transfer* 34 (1998) 101–105. <https://doi.org/10.1007/s002310050236>.
- [4] M.K. Heshmati, H.D. Khiavi, J. Dehghannya, H. Baghban, 3D simulation of momentum, heat and mass transfer in potato cubes during intermittent microwave-convective hot air drying, *Heat Mass Transfer* (2022). <https://doi.org/10.1007/s00231-022-03256-5>.
- [5] X. Li, M. Farid, A review on recent development in non-conventional food sterilization technologies, *Journal of Food Engineering* 182 (2016) 33–45. <https://doi.org/10.1016/j.jfoodeng.2016.02.026>.
- [6] L. Zhao, B. Bhatia, L. Zhang, E. Strobach, A. Leroy, M.K. Yadav, S. Yang, T.A. Cooper, L.A. Weinstein, A. Modi, S.B. Kedare, G. Chen, E.N. Wang, A Passive High-Temperature High-Pressure Solar Steam Generator for Medical Sterilization, *Joule* 4 (2020) 2733–2745. <https://doi.org/10.1016/j.joule.2020.10.007>.
- [7] D. Barcelo, An environmental and health perspective for COVID-19 outbreak: Meteorology and air quality influence, sewage epidemiology indicator, hospitals disinfection, drug therapies and recommendations, *Journal of Environmental Chemical Engineering* 8 (2020) 104006. <https://doi.org/10.1016/j.jece.2020.104006>.
- [8] A. Fadaei, Ventilation Systems and COVID-19 Spread: Evidence from a Systematic Review Study, *EUR J SUSTAIN DEV RES* 5 (2021) em0157. <https://doi.org/10.21601/ejosdr/10845>.
- [9] Q. Xie, H. Lu, X. Wang, Y. Zhang, N. Zhou, Functionalized hollow mesoporous silica for detection of *Staphylococcus aureus* and sterilization, *Journal of Environmental Chemical Engineering* 9 (2021) 105892. <https://doi.org/10.1016/j.jece.2021.105892>.
- [10] F. Shi, M. Ding, H. Tong, Y. Yang, J. Zhang, L. Wang, H. Li, Y. Huo, Photoelectrocatalytic sterilization on thorn-like ZIF-67/ZnO hybrid photoanodes, *Journal of Environmental Chemical Engineering* 10 (2022) 107385. <https://doi.org/10.1016/j.jece.2022.107385>.
- [11] R. Kumar, A. Rana, Basic Concepts of Sterilization Techniques, *Research Journal of Pharmacology and Pharmacodynamics* 13 (2021) 155–161. <https://doi.org/10.52711/2321-5836.2021.00029>.
- [12] M.G. Stanford, J.T. Li, Y. Chen, E.A. McHugh, A. Liopo, H. Xiao, J.M. Tour, Self-Sterilizing Laser-Induced Graphene Bacterial Air Filter, *ACS Nano* 13 (2019) 11912–11920. <https://doi.org/10.1021/acsnano.9b05983>.
- [13] M. Raeiszadeh, B. Adeli, A Critical Review on Ultraviolet Disinfection Systems against COVID-19 Outbreak: Applicability, Validation, and Safety Considerations, *ACS*

- Photonics 7 (2020) 2941–2951.
<https://doi.org/10.1021/acsp Photonics.0c01245>.
- [14] A. Sakudo, Y. Yagyu, T. Onodera, Disinfection and Sterilization Using Plasma Technology: Fundamentals and Future Perspectives for Biological Applications, *IJMS* 20 (2019) 5216.
<https://doi.org/10.3390/ijms20205216>.
- [15] T. Uppal, A. Khazaiehi, A.M. Snijders, S.C. Verma, Inactivation of Human Coronavirus by FATHHOME's Dry Sanitizer Device: Rapid and Eco-Friendly Ozone-Based Disinfection of SARS-CoV-2, *Pathogens* 10 (2021) 339.
<https://doi.org/10.3390/pathogens10030339>.
- [16] M. Busto, E.E. Tarifa, M. Cristaldi, J.M. Badano, C.R. Vera, Simulation of thermal sanitization of air with heat recovery as applied to airborne pathogen deactivation, *Int. J. Environ. Sci. Technol.* (2022).
<https://doi.org/10.1007/s13762-022-03948-9>.
- [17] E.M. Darmady, K.E.A. Hughes, J.D. Jones, D. Prince, W. Tuke, Sterilization by dry heat, *Journal of Clinical Pathology* 14 (1961) 38–44.
<https://doi.org/10.1136/jcp.14.1.38>.
- [18] S. Riddell, S. Goldie, A. Hill, D. Eagles, T.W. Drew, The effect of temperature on persistence of SARS-CoV-2 on common surfaces, *Virol J* 17 (2020) 145.
<https://doi.org/10.1186/s12985-020-01418-7>.
- [19] T.F. Yap, Z. Liu, R.A. Shveda, D.J. Preston, A predictive model of the temperature-dependent inactivation of coronaviruses, *Appl. Phys. Lett.* 117 (2020) 060601.
<https://doi.org/10.1063/5.0020782>.
- [20] K. Ghasemi, S. Tasnim, S. Mahmud, Second law analysis of pillow plate heat exchanger to enhance thermal performance and its simulation studies, *Heat Mass Transfer* (2022).
<https://doi.org/10.1007/s00231-022-03245-8>.
- [21] J. Jiménez, Computers and turbulence, *European Journal of Mechanics - B/Fluids* 79 (2020) 1–11.
<https://doi.org/10.1016/j.euromechflu.2019.06.010>.
- [22] S. Sarkar, B. Lakshmanan, Application of a Reynolds stress turbulence model to the compressible shear layer, *AIAA Journal* 29 (1991) 743–749.
<https://doi.org/10.2514/3.10649>.
- [23] S. Mirfendereski, A. Abbassi, M. Saffar-avval, Experimental and numerical investigation of nanofluid heat transfer in helically coiled tubes at constant wall heat flux, *Advanced Powder Technology* 26 (2015) 1483–1494.
<https://doi.org/10.1016/j.apt.2015.08.006>.
- [24] M. Marion, R. Temam, Navier-stokes equations: Theory and approximation, in: *Handbook of Numerical Analysis*, Elsevier, 1998: pp. 503–689.
[https://doi.org/10.1016/S1570-8659\(98\)80010-0](https://doi.org/10.1016/S1570-8659(98)80010-0).
- [25] B.E. Rapp, Continuity and Navier-Stokes Equations in Different Coordinate Systems, in: *Microfluidics: Modelling, Mechanics and Mathematics*, Elsevier, 2017: pp. 303–308.
<https://doi.org/10.1016/B978-1-4557-3141-1.50013-7>.
- [26] N.A. Che Sidik, S.N.A. Yusuf, Y. Asako, S.B. Mohamed, W.M.A. Aziz Japa, A Short Review on RANS Turbulence Models, *CFDL* 12 (2020) 83–96.
<https://doi.org/10.37934/cfdl.12.11.8396>.
- [27] N.D. Katopodes, Turbulent Flow, in: *Free-Surface Flow*, Elsevier, 2019: pp. 566–650.
<https://doi.org/10.1016/B978-0-12-815489-2.00008-3>.
- [28] S. Fu, L. Wang, RANS modeling of high-speed aerodynamic flow transition with consideration of stability theory, *Progress in Aerospace Sciences* 58 (2013) 36–59.
<https://doi.org/10.1016/j.paerosci.2012.08.004>.
- [29] H. Mandler, B. Weigand, On frozen-RANS approaches in data-driven turbulence modeling: Practical relevance of turbulent scale consistency during closure inference and application, *International Journal of Heat and Fluid Flow* 97 (2022) 109017.
<https://doi.org/10.1016/j.ijheatfluidflow.2022.109017>.
- [30] X. Lei, Z. Guo, Y. Wang, H. Li, Assessment and improvement on the applicability of turbulent-Prandtl-number models in RANS for liquid metals, *International Journal of Thermal Sciences* 171 (2022) 107260.
<https://doi.org/10.1016/j.ijthermalsci.2021.107260>.
- [31] D. Jiang, H. Zhang, W. Yao, Z. Zhao, M. Gui, Z. Chen, The control mechanisms of electromagnetic force for turbulent channel flow with sinusoidal wall deformation, *Ocean Engineering* 260 (2022) 112069.
<https://doi.org/10.1016/j.oceaneng.2022.112069>.
- [32] J. Fröhlich, D. von Terzi, Hybrid LES/RANS methods for the simulation of turbulent flows, *Progress in Aerospace Sciences* 44 (2008) 349–377.
<https://doi.org/10.1016/j.paerosci.2008.05.001>.
- [33] S. Heinz, A review of hybrid RANS-LES methods for turbulent flows: Concepts and

- applications, *Progress in Aerospace Sciences* 114 (2020) 100597.
<https://doi.org/10.1016/j.paerosci.2019.100597>.
- [34] A.V. Rodionov, On the use of Boussinesq approximation in turbulent supersonic jet modeling, *International Journal of Heat and Mass Transfer* 53 (2010) 889–901.
<https://doi.org/10.1016/j.ijheatmasstransfer.2009.11.035>.
- [35] B.E. Launder, D.B. Spalding, THE NUMERICAL COMPUTATION OF TURBULENT FLOWS, in: *Numerical Prediction of Flow, Heat Transfer, Turbulence and Combustion*, Elsevier, 1983: pp. 96–116.
<https://doi.org/10.1016/B978-0-08-030937-8.50016-7>.
- [36] B.E. Launder, B.I. Sharma, APPLICATION OF THE ENERGY-DISSIPATION MODEL OF TURBULENCE TO THE CALCULATION OF FLOW NEAR A SPINNING DISC, 1 (n.d.) 8.